Journal of Nuclear Materials 526 (2019) 151779

Contents lists available at ScienceDirect

Journal of Nuclear Materials

journal homepage: www.elsevier.com/locate/jnucmat

Microbeam synchrotron radiation diffraction and fluorescence of oxide layers formed on zirconium alloys at different corrosion temperatures

Brendan Ensor [a, b, *], David J. Spengler [b], John R. Seidensticker [c], Ram Bajaj [c], Zhonghou Cai [d], Arthur T. Motta [a]

[a] Department of Mechanical and Nuclear Engineering, The Pennsylvania State University, University Park, PA, 16802, USA
[b] Naval Nuclear Laboratory, Schenectady, NY, 12309, USA
[c] Naval Nuclear Laboratory, West Mifflin, PA, 15122, USA
[d] Advanced Photon Source, Argonne National Laboratory, Argonne, IL, 60439, USA

HIGHLIGHTS

- Studied Zircaloy-4 oxide layers corroded at a range of temperatures (274°C–427 °C) at the APS.
- μXRD/XRF of oxide crystal structures showed a preferred orientation to minimize growth stress.
- The monoclinic oxide grain size increased with corrosion temperature; the tetragonal grain size did not.
- Away from the MOI and above a critical size, the tetragonal grains transform into monoclinic grains.
- This variation in tetragonal phase fraction was linked with stress in the oxide.

GRAPHICAL ABSTRACT

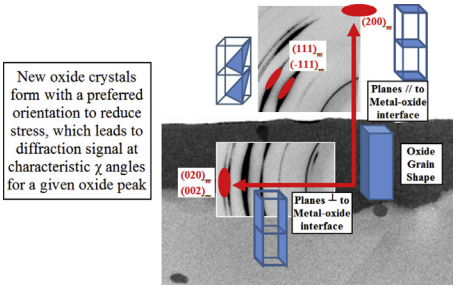

ARTICLE INFO

Article history:
Received 15 March 2019
Received in revised form
13 July 2019
Accepted 29 August 2019
Available online 3 September 2019

Keywords:
Zirconium alloy
Zircaloy-4
Corrosion
Synchrotron radiation

ABSTRACT

Autoclave corrosion tests of Zircaloy-4 were performed at temperatures ranging from 274°C to 427 °C to determine how the characteristics of the oxide layer changed with corrosion temperature. Corroded samples were prepared in cross-section and examined at the Advanced Photon Source using x-ray diffraction and fluorescence with sub-micron spatial resolution. These measurements provide high fidelity data for characterization of the oxide layer grown on zirconium alloys over a range of temperatures to better understand the fundamental mechanisms of corrosion. It was found that the size of the monoclinic oxide grains increases with distance from the metal-oxide interface, while the average grain size of the tetragonal oxide phase decreases. This is consistent with the continuous nucleation of a mixture of equiaxed tetragonal and monoclinic grains at the metal-oxide interface, of which only the monoclinic oxide grains that are properly aligned to minimize stresses grow into long columnar oxide grains. The tetragonal phase oxide grains transform to monoclinic oxide once a critical size is reached. While the monoclinic oxide grain size increases with corrosion temperature, the tetragonal phase grain size remains below a maximum value. Evolution of the tetragonal fraction, calculated with the Garvie-

* Corresponding author. PO Box 1072, Mail Stop 102, Schenectady, NY 12301-1072, USA.
E-mail address: brendan.ensor@unnpp.gov (B. Ensor).

https://doi.org/10.1016/j.jnucmat.2019.151779

Nicholson formula, was observed, with local maxima seen just before transition and local minima seen at oxide locations corresponding to the oxide kinetic transition. No difference was observed in the tetragonal phase fraction in the oxide layers formed at different corrosion temperatures. Detailed fluorescence and diffraction mapping of one sample showed the evolution of the diffraction intensity over a short range in the oxide. This work provides a systematic study revealing fundamental characteristics of the microstructure of Zircaloy-4 oxide layers to further understanding of corrosion resistance of these materials.

1. Introduction

Zirconium alloys are widely used in water-cooled nuclear reactors as fuel cladding due to their low neutron cross-section, suitable mechanical properties, and excellent corrosion resistance. Corrosion resistance in these alloys is important because the coolant temperature in a typical nuclear reactor is as high as 360 °C at pressures as high as 15.5 MPa. These alloys remain in these harsh conditions for years with corrosion and the associated hydrogen uptake as one of the main factors that limit nuclear fuel cladding in service [1]. Therefore the fuel cladding should be as resistant to corrosion as practically possible.

In spite of the importance of zirconium alloys developed through decades of research, a thorough understanding of the corrosion mechanism is yet to be achieved [2,3]. It is known during corrosion of properly designed alloys, a protective oxide layer is formed which slows further oxidation [1–4]. The protective oxide layer is constituted mostly of monoclinic phase ZrO_2 with minor amounts of tetragonal phase ZrO_2. Although the tetragonal phase of the oxide is not normally stable in the typical environment of a nuclear reactor, it can be stabilized by small oxide grain size, by the presence of alloying elements, and by high compressive stresses in the oxide that result from the imperfect accommodation of the volume difference between the metal consumed and the oxide formed [5–7].

At a critical point in the oxide growth (characteristic of each alloy in a given environment), a kinetic transition can take place during which the oxide layer loses its protective character, allowing easy water ingress, and causing the corrosion rate to increase. The newly formed oxide again becomes protective slowing the oxidation until it reaches a new transition, in a cyclic process [8]. The corrosion kinetics have been previously described by a power law and in between transitions the power exponent has been measured to be somewhere between sub-cubic and parabolic, depending on the alloy composition and the environment it corrodes in [8–10]. The cause of the kinetic transition is presently unknown, although a number of mechanisms have been proposed [5,6,10,11].

The microstructure of the oxide formed, and its evolution during corrosion, has been considered to be a key parameter for corrosion kinetics of Zr alloys. The work presented here attempts to help answer some of these questions by examining oxide microstructure characteristics on samples before and after the first kinetic transition primarily as a function of corrosion temperature using synchrotron x-ray diffraction. In particular, a link between the tetragonal phase fraction and the stress in the oxide is discussed in this paper. While an understanding of the general characteristics of the oxide microstructure exists, this paper describes experiments systematically performed on samples corroded in autoclave to various oxide thicknesses and the changes in the oxide microstructure characteristics that result from the wide range of corrosion temperatures examined.

2. Experimental techniques and methods

Microbeam synchrotron radiation permits investigation of the oxide at precise locations, allowing for high spatial and energy resolution [9,10,12]. The Advanced Photon Source (APS) at Argonne National Laboratory (ANL) has been used in a number of studies due to the high brilliance of its x-ray beam and to the ability of focusing it to a sub-micron spot [9,10,12–14]. The 2-ID-D beamline permits tunable energy from 5 to 32 keV and micro x-ray diffraction (XRD) and fluorescence with a nominal spot size of 0.2 μm × 0.2 μm. As the microbeam is scanned across the oxide, the simultaneous acquisition of structural information from XRD and elemental information from x-ray fluorescence (XRF) can be used to analyze the specimens. A schematic depiction of the experimental setup at the 2-ID-D beamline used in this work is shown in Fig. 1.

The composition of Zircaloy-4 used in this study is 1.2–1.7 wt% Sn, 0.18–0.24 wt% Fe, 0.07–0.13 wt% Cr, and 1000–1400 ppm oxygen with the remainder as zirconium [1]. Oxidized samples were prepared by cutting coupons into small pieces which were placed into a slotted molybdenum rod, which was then secured inside a brass tube using epoxy (EpoTek 353ND), as done previously [13–15]. The tube was cured overnight then cut into ~1–2 mm thick disks, which were polished to a mirror finish. An example of a sample ready to be examined using synchrotron radiation is shown in Fig. 2.

Fig. 2 (a) shows an optical micrograph of a sample encased as described above. Fig. 2 (b) shows a cross-sectional SEM micrograph of the oxide layer and the Zircaloy-4 metal. Similar samples were prepared for all the specimens listed in Table 1. The 2-ID-D beamline at the APS at ANL was used to examine 16 unique samples from the 11 different materials, listed in Table 1.

The nine samples in Table 1 that were tested in the recrystallized alpha annealed condition (Rx α-annealed) were processed using a thermomechanical treatment which resulted in a microstructure containing equiaxed grains of ~15 μm and large intragranularly distributed globular second phase particles (average diameter of 0.24 μm), as shown in Fig. 2 (b) [16,17]. The β-quench thermomechanical treatment led to a Widmanstätten-type structure. Two samples were prepared in the β-quenched and annealed condition. These samples exhibited smaller precipitates of irregular shape concentrated at the lath boundaries [18]. The Kearns factor (resolved fraction of basal poles aligned in the normal direction) for the two base metal textures were widely different: f~0.6 for Rx α-annealed and f~0.33 for β-quenched samples [13,14,19]. The samples were corroded in an autoclave in pure water at a variety of temperatures in the range 274°C–427 °C. The weight gain changes during corrosion for the samples in Table 1 are shown in Fig. 3.

During the experiment, each sample was attached onto an aluminum stud which was tilted into the beam's path, causing it to hit the sample at an incident angle of 14° as done previously [9,14]. This created a 0.2 μm × 1.0 μm beam footprint, with the smaller dimension along an axis perpendicular to the metal-oxide

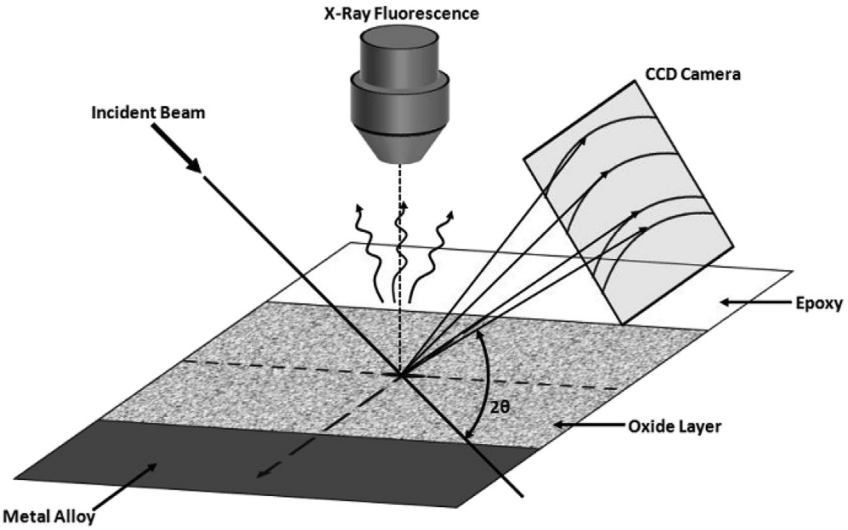

Fig. 1. Schematic of the experimental geometry at the 2-ID-D beamline at the APS. The incident beam comes in at a 14° angle into the material. The fluorescence detector and diffraction detector simultaneously capture data. The small spot size (approximately 0.2 μm × 1 μm due to geometry) permits precise spatial investigation of the material examined [13,14].

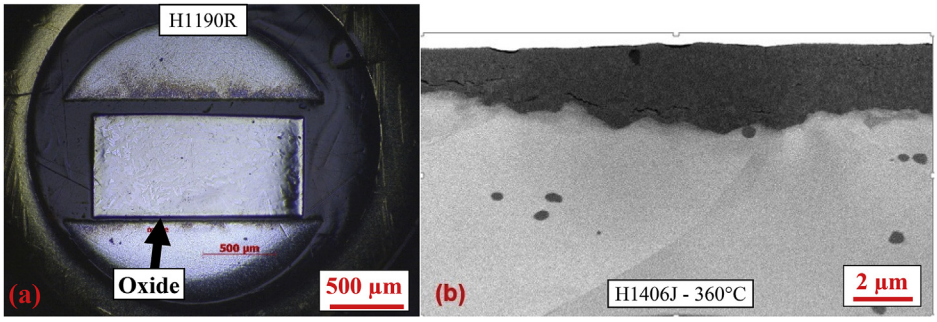

Fig. 2. (a) Cross-sectional Zircaloy-4 sample H1190R (274 °C, 2.35 μm); the brass tube is on the outside, and the Zircaloy-4 sample sits inside the slotted molybdenum rod, the oxide is on the bottom and cannot be seen in this image. (b) SEM image of (H1406J (Zircaloy-4, 360 °C for 120 days) taken using a FEI Helios NanoLab™ 660 SEM/FIB showing the oxide (dark gray) and the metal (light gray). Second-phase precipitates (SPP) are visible in the metal matrix.

Table 1
List of samples corroded in autoclave and tested at the 2-ID-D beamline at the APS.

Material ID	Alloy	Corrosion Environment[a]	Time (days)	Oxide thickness (μm)[b]	Heat Treatment [16]
H2287J	Zircaloy-4	274 °C water	3003	2.05 μm	Rx α-annealed
H1190R	Zircaloy-4	274 °C water	3003	2.35 μm	β-quenched
N2513	Zircaloy-4	316 °C water	3113	13.1 μm	Rx α-annealed
H1405J	Zircaloy-4	360 °C water	20	1.14 μm	Rx α-annealed
H1406J	Zircaloy-4	360 °C water	120	2.09 μm	Rx α-annealed
H1372J	Zircaloy-4	360 °C water	170	4.02 μm	Rx α-annealed
H1187R	Zircaloy-4	360 °C water	170	3.03 μm	β-quenched
H1312J	Zircaloy-4	400 °C steam	41.3	3.5 μm	Rx α-annealed
H1313J	Zircaloy-4	400 °C steam	259.4	9.1 μm	Rx α-annealed
H3035J	Zircaloy-4	413 °C steam	210	7.81 μm	Rx α-annealed
H3017J	Zircaloy-4	427 °C steam	203	13.6 μm	Rx α-annealed

[a] H2287J, H1190R, H1312J, H1313J, H3017J, and H3035J were corroded for 3 days in 360 °C water prior to listed exposure, <0.8 μm of oxide.
[b] Oxide thickness reported is the average oxide thickness based on sample weight gain.

interface. All the samples were examined using a beam energy of 8.34 keV with a few samples examined at an energy of 10.1 keV. The size and location of the charge-coupled device (CCD) detector allowed recording diffraction peaks within the 2θ range of 20°–42°, which at 8.34 keV, encompassed planes with d-spacings between ~2 and 4 Å, corresponding to a wide range of diffraction peaks from the phases of interest. A Ge (Li) Canberra solid state detector was used to acquire fluorescence data at each step. When placed onto the oxide layer the incident x-ray beam generates about 4/5 of the Zr fluorescence counts it generates when placed on the metal, which allowed determination of the beam position within the layer quite precisely, as shown in Fig. 4. The metal-oxide interface could be determined from the mid-point of the sloped region between the metal and oxide, while the oxide-water interface was set at the

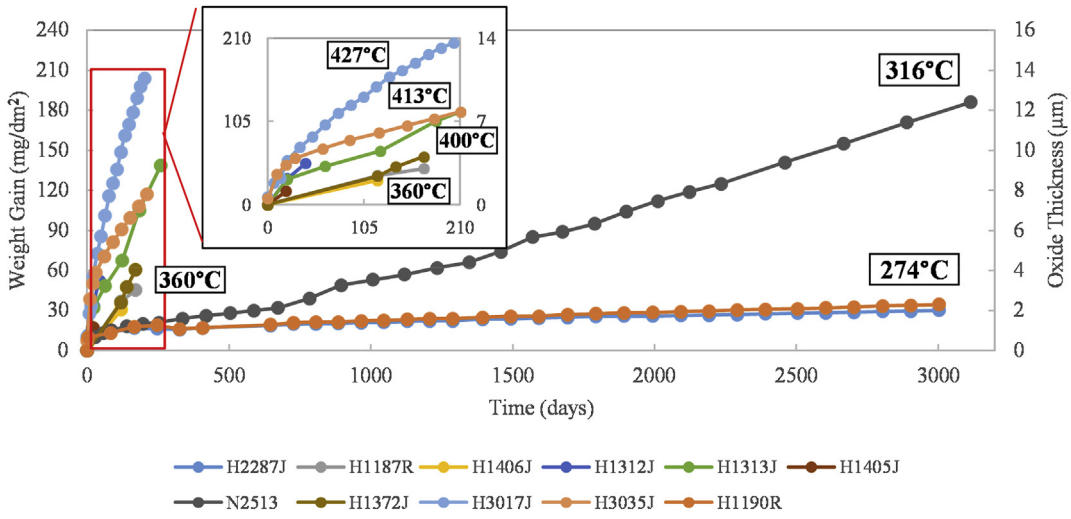

Fig. 3. Weight gain data for the 11 specimens examined by XRD at the 2-ID-D beamline at the APS. The region highlighted in the rectangle is shown in the inset. Each sample was examined at the last data point on the curve.

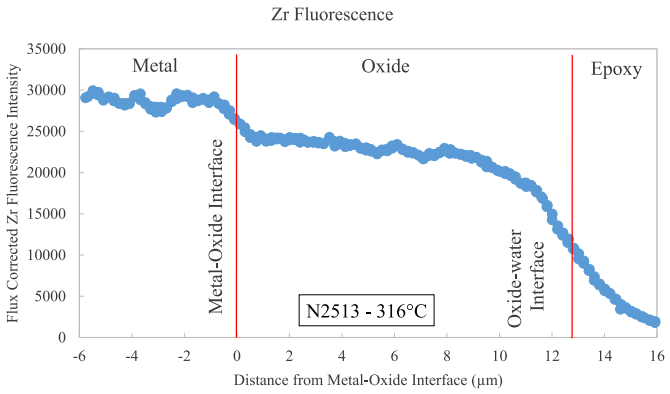

Fig. 4. Example of the zirconium fluorescence counts taken from the oxide layer and metal in the sample N2513 (316 °C, 13.1 μm, see Table 1) acquired at the 2-ID-D beamline at the APS and used to determine the location of the metal-oxide and oxide-water interfaces.

location where the intensity dropped to half the value from within the oxide.

The microbeam moves across the oxide layer in steps of 0.1–0.25 μm. For each sample, multiple scans were acquired to account for variations at different locations within the oxide [13,14]. Over 70 scans and 3,000 diffraction patterns were analyzed for this study. An example of a raw diffraction pattern acquired is shown in Fig. 5, highlighting the 2θ and chi (χ) directions. The diffraction patterns themselves were viewed using the ImageJ program [20]. A chi range of approximately ~110° was acquired (depending on the specific diffraction peak). The remaining pattern was obscured by the sample and the mounting geometry. The reflection XRD geometry combined with the ~110° χ range lead to the bulk of the diffraction intensity being from planes that were perpendicular to the metal-oxide interface (i.e. out-of-plane).

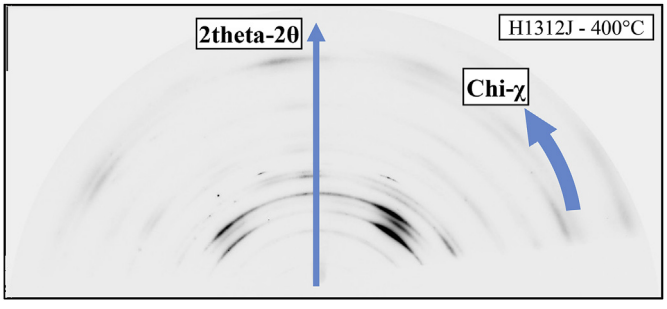

Fig. 5. Example of diffraction pattern taken from a location in the oxide layer formed on sample H1312J (400 °C, 3.5 μm); the 2θ and χ directions are illustrated as well.

Diffraction patterns such as that shown in Fig. 5 were integrated over the entire diffraction arc (the χ angle) using either the *CCD sum Sdiapp* or *Fit2D* computer programs [13,21]. The resulting integrated patterns were imported into Microsoft Office Excel and MATLAB for background removal. The data was then brought into the *PeakFit* computer program for diffraction peak fitting and analysis [22]. The peaks were manually fit using the Pearson VII peak shape which allows both peak height and full-width half-maximum (FWHM) to be adjusted, as done previously [9,14]. Typical R^2 values for the overall fits were above 0.98 for low intensity profiles and 0.995 for typical bulk oxide profiles. An example of such a fit can be seen in Fig. 6. The fits were then collectively compiled using an Excel macro for a variety of analyses of the changing diffraction patterns within the oxide layer.

3. Results

Diffraction peaks corresponding to both the monoclinic and tetragonal phases of ZrO_2 were identified from the diffraction patterns taken from the oxide layers studied. As shown in the table in Fig. 6, the oxide peaks matched well with their predicted 2θ locations based on d-spacings listed in the powder diffraction files (#05–0665, #37–1484, #42–1164, and #22–1025). The only exception was the $(101)_t$ tetragonal peak as noted below. The primary planes corresponding to monoclinic ZrO_2 observed were the $(111)_m$, $(\bar{1}11)_m$ peaks (also the highest intensity peaks in the powder diffraction files), as well as the peaks in the $\{200\}_m$ family. Relatively lower intensity monoclinic planes observed included the $(011)_m$, $(110)_m$, $(102)_m$, $(012)_m$, $(112)_m$, $(201)_m$, and $(\bar{1}21)_m$. Only one plane corresponding to tetragonal ZrO_2 could be identified, the $(101)_t$ (observed at a lower d-spacing than the literature value, as previously seen) [9,10,13,14]. Although there was some evidence for the presence of the $(002)_t$ peak, particularly near the metal-oxide interface of some oxide layers, it was nearly coincident with

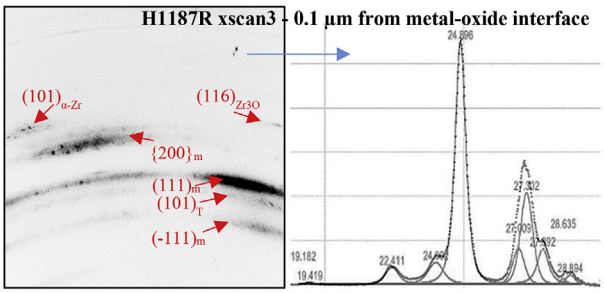

Phase	Orientation	Observed 2θ	Expected 2θ*	% Δ
Monoclinic	(1 1 0)	19.18	19.11	0.36
Monoclinic	(0 1 1)	19.42	19.42	0.0
Monoclinic	(-1 1 1)	22.41	22.36	0.22
Tetragonal	(1 0 1)	24.00	23.65	1.45
Monoclinic	(1 1 1)	24.90	24.95	0.20
Monoclinic	(2 0 0)	27.01	27.07	0.22
Monoclinic	(0 2 0)	27.30	27.25	0.18
Monoclinic	(0 0 2)	27.90	27.89	0.04
Zr_3O	(1 1 6)	28.64	28.69	0.17
α-Zirc	(1 0 1)	28.89	28.91	0.07

Fig. 6. Example of the integration and fitting of the diffraction patterns obtained at the 2-ID-D beamline at the APS at 10.1 keV (energy used for the data shown). The pattern is from sample H1187R (360 °C, 3.03 μm) and was obtained in the oxide layer near the metal-oxide interface, so both metal and suboxide intensities are seen. *From PDF (#05–0665, #37–1484, #42–1164, and #22–1025).

nearby $\{200\}_m$ peaks and could not be positively identified. The $(101)_t$ peak normally appeared aligned with the $(111)_m$ and $(\bar{1}11)_m$ peaks on the diffraction patterns (as seen in Fig. 6). It was visible as a shoulder on the low 2θ side of the $(111)_m$ peak of the integrated diffraction patterns. Additionally, peaks that could be indexed as the Zr_3O suboxide phase were seen in the metal just ahead of the metal-oxide interface, typically in samples in which the oxide layers were close to the oxide kinetic transition [23]. The most prominent suboxide peak corresponded to the diffraction from the $(116)_{Zr3O}$ plane.

The set of samples selected for analysis at the APS allowed a systematic study of the differences in the microstructure of oxide layers formed on zirconium alloys during corrosion at different temperatures (274 °C–427 °C). For every diffraction pattern acquired during each scan the following parameters were determined from the results of the diffraction pattern fitting: integrated peak areas, peak positions, and breadth (FWHM). From these results the tetragonal phase fraction from the Garvie-Nicholson formula and the oxide grain size were calculated.

The characteristic size of the monoclinic and tetragonal grains formed in the oxide was calculated using the Debye-Scherrer equation [9]. This calculation assumes that all peak broadening caused by the sample is due to size broadening (rather than to strain broadening). In the geometry used, the calculated size corresponds to the width of the long columnar monoclinic phase oxide grains and to the diameter of the equiaxed oxide grains. The Debye-Scherrer equation, calculates the grain size d from the FWHM of the peaks discerned from the fitted diffraction patterns [9]:

$$d = \frac{0.9\lambda}{B_\theta cos\theta} \quad \text{where} \quad B_\theta = \left(B^2 - B_i^2\right)^{1/2} \tag{1}$$

where B is the measured peak FWHM in radians, and B_i is the instrumental broadening, which was measured to be 0.051 radians in this beamline using a LaB_6 standard, λ is the wavelength and θ is the diffraction angle.

The tetragonal fraction, f_T, was calculated from the Garvie-Nicholson formula where each term represents the integrated area of the specific crystallographic peak of the oxide phase denoted [24]:

$$f_t = \frac{I(101)_t}{I(101)_t + I(\bar{1}11)_m + I(111)_m} \tag{2}$$

For experiments with samples in which a smaller χ range was acquired, a texture correction was applied, as done previously [9,13,14]. This texture-corrected tetragonal fraction uses coefficients of 2.2, 0.88, and 25 as multipliers to the $(101)_t$, $(111)_m$, and $(\bar{1}11)_m$ peak intensities, respectively.

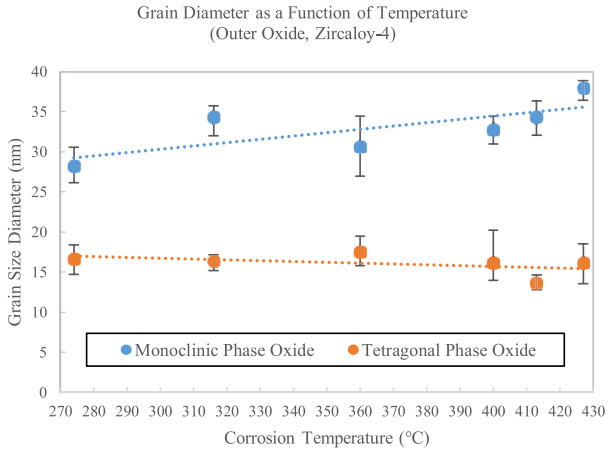

Fig. 7. Average oxide grain diameter for each temperature calculated from the Debye-Scherrer equation of an average of the major monoclinic orientations and the $(101)_T$ orientation for the tetragonal oxide, for Zircaloy-4 with oxide >2 μm; error bars indicate minimum and maximum scan averages in addition to measurement error.

3.1. Oxide layer grain size

Using x-ray diffraction the oxide grain size was calculated from the Debye-Scherrer equation from the broadening of five different monoclinic oxide peaks and from the $(101)_t$ peak using Equation (1).[1] The grain sizes calculated by this method were averaged across the whole oxide layer for an individual scan. Fig. 7 shows the grain diameter calculated from the average broadening of the five monoclinic peaks and from the $(101)_t$ peak, averaged over the whole oxide layer for the scans performed on the Zircaloy-4 samples corroded at various temperatures from 274°C to 427 °C. The plot shows that as the corrosion temperature increases, the average monoclinic grain size increases, as would be expected. This behavior is observed for all monoclinic oxide peaks for which grain size was calculated. In contrast, the tetragonal grain size remains essentially constant with temperature at close to 15 nm. This is consistent with previous literature results which show values in the range of 10–20 nm [9,14,25,26] and theorized stability values based

[1] The calculation performed attributes all the broadening observed to grain size, rather than strain. Although it is recognized that the oxide diffraction peak broadening is also affected by strain, previous analysis using Williamson-Hall plots has shown that for these oxide layers most of the broadening comes from size broadening, justifying this assumption [14].

on free energy [6,27,28]. The fact that the tetragonal grain size does not change with corrosion temperature can be explained if the tetragonal grains transform into monoclinic grains once they reach a critical size. This transformation is helped by the decrease of the stress level in the oxide with distance from the metal-oxide interface, thus helping destabilize the tetragonal phase relative to the monoclinic.

The detailed variation of the grain size with distance from the metal-oxide interface was also studied. Fig. 8 shows the calculated size of the monoclinic and tetragonal grains calculated from the broadening of the $(111)_m$ and $(101)_t$ diffraction peaks as a function of distance from the metal-oxide interface for the two highest and lowest water corrosion temperatures, 274 °C and 360 °C. For Fig. 8, oxides that have just undergone transition and with roughly the same oxide thickness are compared for four samples at two corrosion temperatures (274 °C - blue and 360 °C - green), which demonstrate the consistency of the observations. While the monoclinic grain size increases with distance from the metal-oxide interface, the tetragonal grain size decreases to a size of ~15 nm, again consistent with a transformation of the large tetragonal grains to monoclinic when they are above a certain size and are away from the metal-oxide interface. It is also seen that the monoclinic grains are larger for oxide layers formed at the higher corrosion temperature while the tetragonal grain size is unchanged.

3.2. Tetragonal phase fraction

As shown in Equation (2), the tetragonal phase fraction calculation is based on the areas of three oxide peaks, $(101)_t$, $(-111)_m$, and $(111)_m$. These peaks are typically observed at approximately the same χ angle on the diffraction patterns, (indicating they are aligned with one another). It has been proposed that the χ angle (such as observed in the diffraction pattern in Fig. 6) at which these peaks were typically observed is determined by a preferred orientation of the oxide to reduce stress. The preferential oxide orientation has been previously shown to have anywhere from the $(-301)_m$ to the $(-601)_m$ planes parallel to the oxide growth direction [29]. This is reasonably close to the orientation of the $(200)_m$ plane and consistent with the observations in this study. The observed χ angle of the $(101)_t$, $(-111)_m$, and $(111)_m$ peaks is also consistent with this determination. The $(101)_t$ peak normally

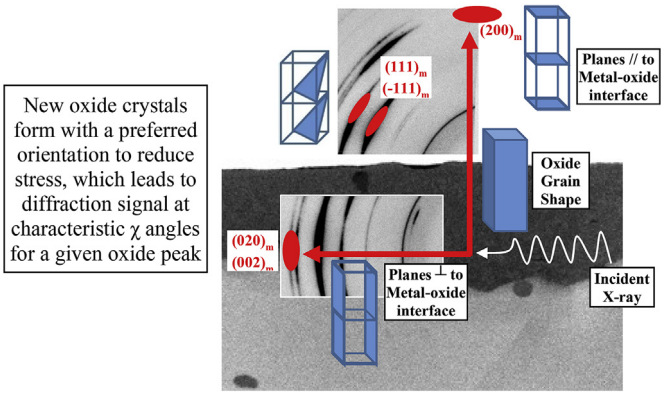

Fig. 9. Sketch of how preferred orientation of oxide growth due to stress leads to characteristic diffraction signal at specific χ angles for a given oxide peak. Illustrated here are the $(111)_m$, $(-111)_m$, $(200)_m$, $(020)_m$, and $(002)_m$ planes and resulting diffraction signals.

appeared aligned with the $(111)_m$ and $(-111)_m$ peaks on the diffraction patterns. Fig. 9 shows a sketch of the preferred orientation of oxide growth and the resulting characteristic diffraction signal at specific χ angles for five oxide peaks. Thus, the results confirm previously proposed crystal structure alignment of the monoclinic oxide relative to the metal. The oxide layer crystal orientation and texture was observed to be the same for oxide layers formed during corrosion of the two different metal textures. Although there were only a few samples examined with the different metal texture, and not enough for a conclusive determination, this would suggest that the developed oxide texture is not strongly dependent on an oxide-matrix orientation relationship, although some work has suggested a relationship between metal texture and the corrosion rate of the oxide formed on a particular grain [30].

The zirconium oxide tetragonal phase fraction, f_T, was calculated for every diffraction pattern obtained using Equation (2). Fig. 10 shows f_T as a function of distance from the metal-oxide interface for five scans obtained from different samples corroded at a range of temperatures from 274°C to 400 °C and a variety of oxide thicknesses. To understand these results it is necessary to consider the possible causes of the variation in f_T. Previous research has shown that the apparent variation in f_T observed in a thick sample

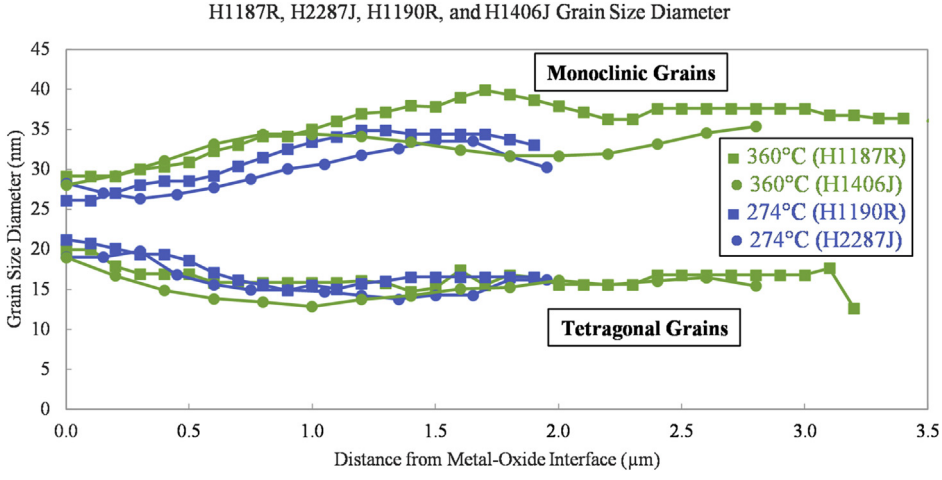

Fig. 8. Grain size calculated from the broadening of the $(111)_m$ and $(101)_t$ oxide peaks versus distance from the metal-oxide interface for four Zircaloy-4 samples; illustrated here are the different behaviors of the oxide phases near the interface. The intensity of the tetragonal phase is lower near the oxide-water interface, occasionally leading to more variability in measurements.

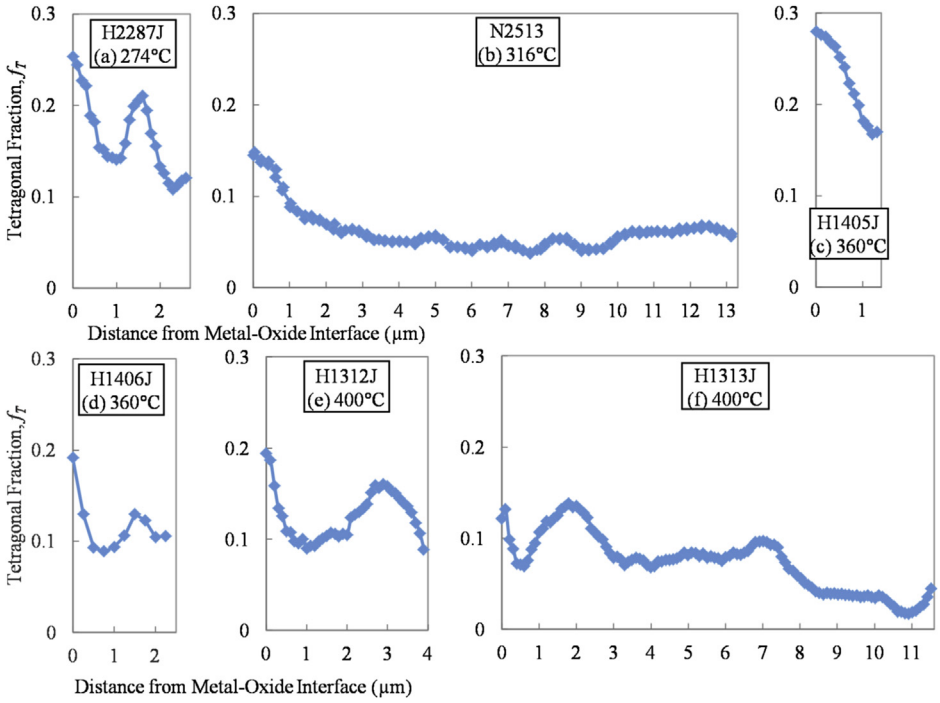

Fig. 10. (a)–(f) Calculated tetragonal fraction in oxide layers formed on recrystallized alpha-annealed Zircaloy-4 samples corroded in water and steam from 274 °C to 400 °C against distance from metal-oxide interface.

with many transitions was caused by a variation in oxide texture, causing the diffracted intensities to show an apparent variation [9]. This was not the case in this work as the integration arc was more comprehensive than in the previous study and the oxide layer texture variations did not influence the calculated tetragonal fraction. The oxide texture observed was similar to previous observations and thus the χ range of ~110° did not influence the results [9,10,14]. It is also possible that the tetragonal phase is stabilized by different factors such as stress, grain size and composition which might vary with distance from the metal-oxide interface. These are discussed below.

More importantly, it is relevant to ask the question as to why study the oxide tetragonal fraction. The motivation to study it in this work was that it could serve as an indicator of stress present. That is, in the absence of other factors, and assuming that the stress present at high temperature is still present when the oxide is cooled down to room temperature for examination, the higher tetragonal fraction can be correlated to a presence of a higher compressive stress, for example at the metal-oxide interface.

For the samples examined, it was consistently observed that: (i) the calculated f_T using Equation (2) was highest at the metal-oxide interface and (ii) in most scans f_T varied within the oxide layer away from the metal-oxide interface. Both of these observations have been previously reported [9,14,31]. The results of the calculations suggest that a minima and maxima in f_T occur in the oxide, which, based on the periodicity, matches what would be expected from a sample going through kinetic transition oxide growth cycles. The calculated f_T are similar for samples corroded in water and in steam. The average f_T among all samples at the metal-oxide interface is approximately ~0.15, decreasing to between 0.05 and 0.1 at a distance above 1.5–2 μm from the metal-oxide interface. Note that the f_T decreases in the region near the metal-oxide interface where the tetragonal grains are transforming to monoclinic grains as shown in Fig. 8.

In order to better understand the behavior of the tetragonal phase in the oxide, particularly the variation within an oxide transition (which can change the value of f_T at the metal-oxide interface), it is useful to plot f_T as a function of distance from the *oxide-water* interface to highlight the behavior of the tetragonal phase when the oxide layer is first formed. Fig. 11 shows a plot of the overall average f_T from all samples, the average f_T from only 360 °C corroded samples, and the average f_T from an individual 360 °C corroded sample at each position as a function of distance from the oxide-water interface. As can be seen, regardless of averaging, the samples show similar behavior. Thus the plot in Fig. 11 is essentially a summary of the data in Fig. 10, that is, a high tetragonal fraction near the interface and an increase in f_T in the oxide before the kinetic transition.

The approximate location of the oxide kinetic transition is highlighted in Fig. 11 by the blue box. As can be seen, in the oxide layer formed right after the oxide kinetic transition the tetragonal fraction increases as the oxide grows towards the next transition and the maxima for each period occurs just prior to the approximate transition locations. With the caveats noted above, it is proposed herein that the tetragonal fraction determined can be used as a record of what the stress at the metal-oxide interface was when the oxide was formed. Thus, the rise in the tetragonal fraction towards the transition point would then be explained by an increase in the stress at the interface as the oxide layer grows. The dip at the transition is thought to be caused by stress relief from plastic deformation and oxide cracking occurring at transition. The resulting stress relief could allow the tetragonal phase to transform to the monoclinic.

The in-plane stress of the tetragonal phase oxide correlates with the f_T calculated as a function of distance from the oxide-water interface, as shown by Swan et al. [31] (see Fig. 10 in Ref. [31]). This is consistent with the observations in this work, where the tetragonal fraction peaks just prior to transition (and there is higher in-plane compressive stress for the tetragonal phase) and then dips to minima where the cracking in the oxide has relieved the stresses.

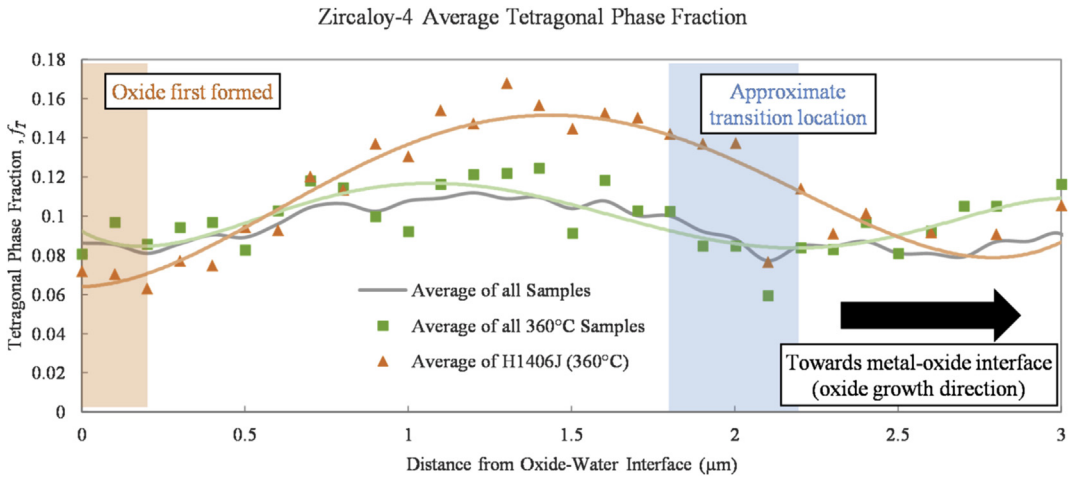

Fig. 11. Average tetragonal fraction as a function of distance from the oxide-water interface for Zircaloy-4 samples; the blue box shows the approximate location in the oxide layer where the oxide kinetic transition is expected to have taken place, and the orange box shows the location of the oxide-water interface. (For interpretation of the references to colour in this figure legend, the reader is referred to the Web version of this article.)

It is hypothesized that the amount of tetragonal phase that forms at the metal-oxide interface increases as transition is approached due to increased oxide growth induced stresses in the metal. Away from the interface, the stresses are lower (but not zero) and some amount of the tetragonal phase transforms to the monoclinic phase. The remnant tetragonal phase left is thus higher for oxide formed closer to transition. However, at the location of the lateral cracking, the stresses are completely relieved and more tetragonal transforms to the monoclinic than away from the cracking. The remnant tetragonal phase fraction observed in fossil oxides is characteristic of this process.

As noted above, the tetragonal phase can also be stabilized by alloying elements and grain size. For these autoclave samples, without exposure to irradiation, the alloying element concentration remains fairly uniform during oxide growth. The alloying elements and small grain size likely provide a background level of tetragonal phase upon which stress can add, since tetragonal phase oxide is observed also in low stress locations. Grain size has previously been linked to tetragonal phase observations [9,23], particularly when the corrosion rate, and thus nucleation rate of new oxide grains, is high. While we have seen some evidence for a higher tetragonal fraction formed at the oxide-water interface in this work (Figs. 10 and 11), the stress stabilization of the tetragonal phase evidenced by the correlation between in-plane compressive stress and the calculated f_T suggests that stress is the dominant contributor to tetragonal phase formation. Finally, variations in diffraction peak intensity due to oxide layer texture could also contribute to variations in the tetragonal phase fraction, but this does not appear to be the case in this instance.

Fig. 12 shows a plot of the average f_T for different temperatures as a function of distance from the metal-oxide interface. The tetragonal fraction does not significantly change with corrosion temperature. If corrosion at higher temperatures occurs following a similar mechanism, only faster, then the data suggest that a higher corrosion rate seen at higher temperature does not necessarily imply a higher tetragonal fraction.

3.3. Diffraction and fluorescence map on Zircaloy-4 sample

To quantify the extent of possible lateral variations in the oxide structure examined, in some of the specimens, scans were set up to sample various locations in the oxide to evaluate the

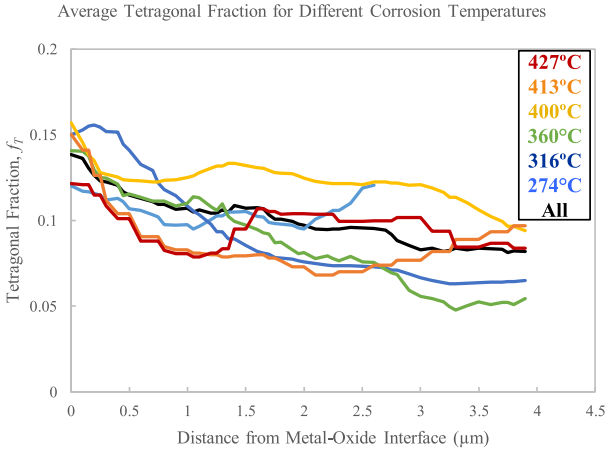

Fig. 12. Average tetragonal fraction in oxide layers formed at different temperatures as a function of distance from the metal-oxide interface for Zircaloy-4 samples; a rolling average over six measurements was used to create these curves.

reproducibility of the oxide characteristics measured. Analysis showed that the relative intensities of monoclinic oxide peaks (which relate to oxide orientation), tetragonal phase fraction, and grain size were similar from scan to scan, i.e. the measurements were reproducible. To determine if this effect was consistent on a

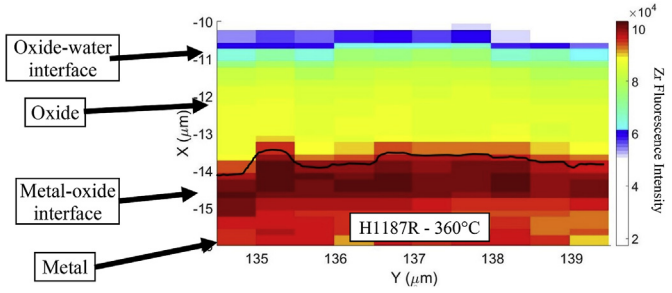

Fig. 13. Zirconium fluorescence for all eleven scans across the oxide in sample H1187R (360 °C, 3.03 μm, Zircaloy-4); each scan is separated by 0.5 μm, step size across the oxide (vertical) is 0.25 μm; metal-oxide interface is drawn as a black line.

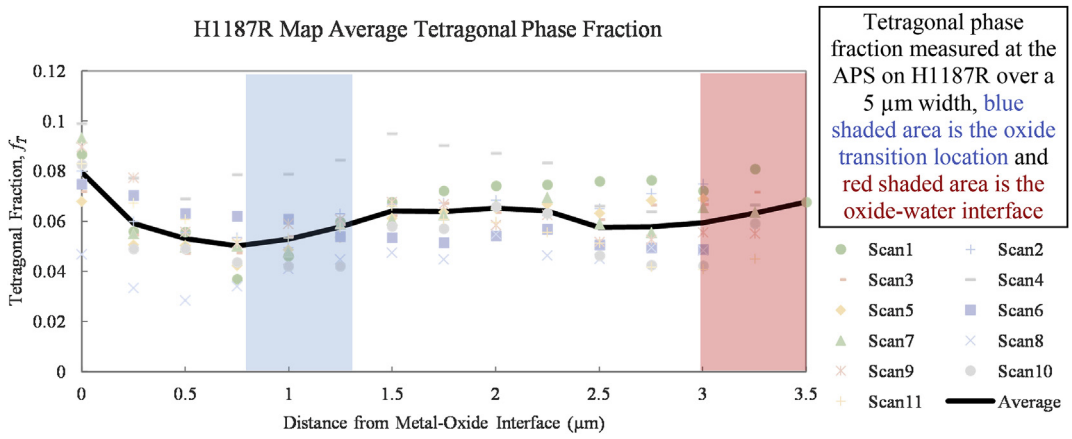

Fig. 14. Average tetragonal phase fraction for all eleven scans across the oxide in sample H1187R (360 °C, 3.03 μm, Zircaloy-4); the red area is the range for the edge of the sample. (For interpretation of the references to colour in this figure legend, the reader is referred to the Web version of this article.)

local scale (i.e. for the oxide layer grown within a single metal grain), a fluorescence map was acquired on one cross-sectional sample consisting of 11 scans set at 0.5 μm apart along the metal-oxide interface and 0.25 μm steps across the oxide. The sample, H1187R (Zircaloy-4, 360 °C, see Table 1), was chosen for its relatively small oxide thickness (3.03 μm), previous experience in experiments, and analysis of the sample that provided assurance in the potential success of the map. The Zr fluorescence intensity is shown in Fig. 13.

The Zr fluorescence map shows the location of metal (bottom-red), oxide (yellow-middle/top), and edge of the sample (blue-top). Additionally, the metal-oxide interface is drawn on the map and is consistent with normal interface variation for this sample. The calculated tetragonal fraction across the layer is similar for all scans and follows the pattern of Figs. 10–12. The average f_T for the map was calculated and is shown in Fig. 14. Similar to Fig. 10 the f_T is highest at the metal-oxide interface with a local maximum in the oxide formed just prior to transition.

Fig. 14 shows: (1) a maximum of the tetragonal fraction at the interface, (2) a slight increase in the tetragonal fraction at the outer surface (far right), and (3) a local maximum in the oxide formed just prior to transition followed by a local minimum at transition, similar to what was shown in Fig. 10. Additionally, it is noteworthy that if the tetragonal fraction is plotted as a function of the oxide thickness, such as in Fig. 15, it is observed that there is a correlation between the thickness of the oxide and f_T.

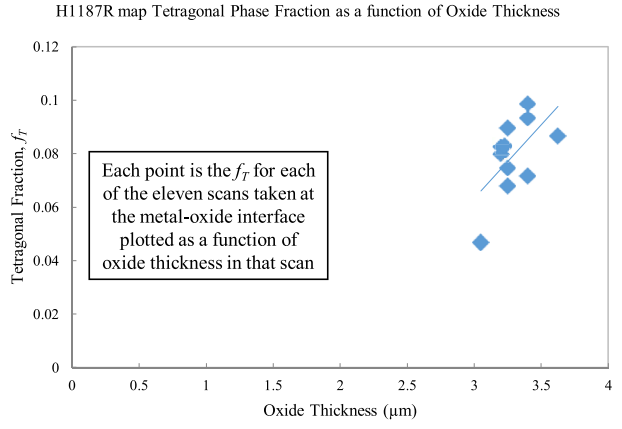

Fig. 15. Tetragonal phase fraction at the metal-oxide interface plotted as a function of oxide thickness for all eleven scans across the oxide in sample H1187R (360 °C, 3.03 μm, Zircaloy-4).

Higher stresses at the metal-oxide interface stabilize the tetragonal phase, particularly larger sized tetragonal phase grains, which lead to the observations on grain size f_T reported in section 3.1 above. As transition is approached and oxide growth stresses build up, it would follow then that there would be more tetragonal phase grains stabilized at the metal-oxide interface than in a section of the oxide layer formed earlier in a transition cycle. Thus, the observations in Fig. 15 that there is a higher f_T in the oxide near the interface for locations of thicker oxide (and presumably closer to transition) is in agreement with the proposition that closer to the oxide transition more tetragonal phase oxide is formed due to the increased stresses present at the metal-oxide interface at that stage. The tetragonal fraction could therefore be used as a record of stress at the metal-oxide interface when the oxide formed.

The observation in Fig. 15 could also be caused by the local heterogeneities in the distribution of the alloying elements (such as Sn). Sn would locally strengthen the metal, thereby causing lower stress accommodation from oxide growth, which could subsequently lead to the formation of more tetragonal phase. Additionally, it could chemically stabilize the tetragonal phase. This relationship between f_T, alloying element concentration, and stress should be studied in more detail.

Fig. 16 shows diffraction patterns and integrated areas of the three oxide peaks contributing to the f_T calculation (arrowed) in a scan of higher f_T (thicker oxide) and a location of lower f_T (thinner oxide). It is clear from Equation (2) that a high f_T can be achieved either by a relatively low intensity of monoclinic peaks or a higher intensity of the tetragonal peak. Fig. 16 shows that the high f_T near the interface is caused by a low value of the monoclinic peaks while that near the transition is caused by a high value of the tetragonal peak.

4. Conclusions

In order to better understand the structure and texture of the oxide layers formed on samples of Zircaloy-4, corroded at a range of temperatures (274°C–427 °C), cross-sectional specimens of oxide layers were examined at the APS using microbeam XRD and XRF in reflection geometry. Results are generally in agreement with previous observations of oxide layers, but provide more detail. The major conclusions are listed below:

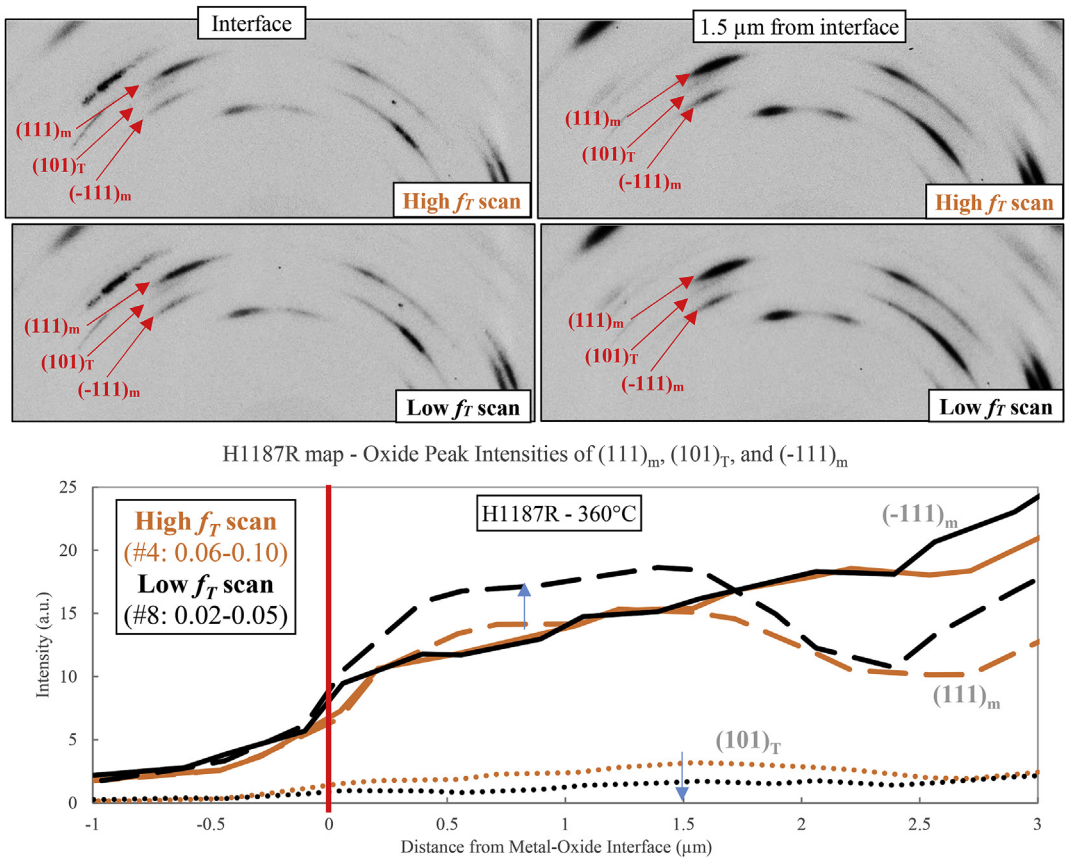

Fig. 16. - Comparison between two scans of sample H1187R (360 °C, 3.03 μm, Zircaloy-4), one with a high f_T and one with a low f_T. On top are diffraction patterns and on the bottom, is the integrated intensity of the diffraction peaks as a function of distance from the metal-oxide interface. As can be seen, the difference in f_T comes from a difference in both the intensity of the tetragonal and monoclinic phases.

Synchrotron XRD-Oxide Orientations

- Both monoclinic and tetragonal phases were identified in the oxide examined. The primary diffraction peaks corresponding to the monoclinic phase observed were the $(111)_m$, $(\bar{1}11)_m$, and the peaks in the $\{200\}_m$ family. Only one diffraction peak corresponding to the tetragonal phase was observed consistently, the $(101)_t$. The orientation of the corresponding peaks in the crystal structure of the growing oxide is consistent with a preferred orientation, characterized by monoclinic grains with the $(200)_m$ plane approximately parallel to the metal-oxide interface, the $(020)_m$ and $(002)_m$ planes perpendicular to the metal-oxide interface, and the $(111)_m$, $(\bar{1}11)_m$, and $(101)_t$ oriented close to a 45° angle with the metal-oxide interface.
- Evidence of the suboxide phase Zr_3O was observed, predominantly near the metal-oxide interface.

Grain Size

- The monoclinic oxide grain size calculated from the broadening of the diffraction peaks increased with corrosion temperature, while the tetragonal grain size did not.
- The observation that the tetragonal oxide grain size does not increase with corrosion temperature is in agreement with the idea that when a critical size is reached the tetragonal grains transform into the monoclinic grains (when no longer stabilized by high stresses near the metal-oxide interface).
- The monoclinic phase grain size is smaller at the metal-oxide interface.
- No effect of metal texture on oxide grain size was observed in the limited number samples examined in this study.

Tetragonal Phase Fraction

- The calculated tetragonal fraction decreases away from a maximum at the metal-oxide interface, with local maxima near the points of the oxide transitions. This variation in tetragonal phase was linked with stress in the oxide.
- The tetragonal fraction does not change significantly with corrosion temperature.
- Within a given oxide kinetic transition cycle, the tetragonal fraction was observed to have a small but consistent increase with the local oxide thickness for one sample over a width of 5 μm.

Data availability

The raw and processed data required to reproduce these findings cannot be shared at this time due to technical or time limitations.

Acknowledgements

This research has been authored by Fluor Marine Propulsion, LLC under Contract No. DOE-89233018CNR000004 with the U.S. Department of Energy. This research used resources of the Advanced Photon Source, a U.S. Department of Energy Office of Science User Facility operated for the DOE Office of Science by Argonne National Laboratory under Contract No. DE-AC02-06CH11357. This research was performed (B. Ensor) under appointment to the Rickover Fellowship Program in Nuclear Engineering sponsored by Naval Reactors Division of the U.S. Department of Energy.

References

[1] C. Lemaignan, A.T. Motta, Zirconium alloys in nuclear applications, in: B.R.T. Frost (Ed.), Materials Science and Technology: A Comprehensive Treatment, 10B, VCH, 1994, pp. 1–51.

[2] T.R. Allen, R.J.M. Konings, A.T. Motta, Corrosion of zirconium alloys, in: R.J.M. Konings (Ed.), Comprehensive Nuclear Materials, vol. 5, Elsevier, Oxford, UK, 2012, pp. 49–68.

[3] A.T. Motta, A. Couet, R.J. Comstock, Corrosion of zirconium alloys for nuclear fuel cladding, Annu. Rev. Mater. Res. 45 (2015) 311–343.

[4] E. Hillner, D.G. Franklin, J.D. Smee, Long-term corrosion of Zircaloy before and after irradiation, J. Nucl. Mater. 278 (2000) 334–345.

[5] B. Cox, Some thoughts on the mechanisms of in-reactor corrosion of zirconium alloys, J. Nucl. Mater. 336 (2005) 331–368.

[6] W. Qin, C. Nam, H.L. Li, J.A. Szpunar, Tetragonal phase stability in ZrO2 film formed on zirconium alloys and its effects n corrosion resistance, Acta Mater. 55 (2007) 1695–1701.

[7] R.C. Garvie, Stabilization of the tetragonal structure in zirconia microcrystals, J. Phys. Chem. 82 (1978) 218–224.

[8] J.S. Bryner, The cyclic nature of corrosionof zircaloy-4 in 633 K water, J. Nucl. Mater. 82 (1979) 84–101.

[9] A. Yilmazbayhan, A.T. Motta, R.J. Comstock, G.P. Sabol, B. Lai, Z. Cai, Structure of zirconium alloy oxides formed in pure water studied with synchrotron radiation and optical microscopy: relation to corrosion rate, J. Nucl. Mater. 324 (2004) 6–22.

[10] A.T. Motta, M.J.G. da Silva, A. Yilmazbayhan, R.J. Comstock, Z. Cai, B. Lai, Microstructural characterization of oxides formed on model Zr alloys using synchrotron radiation, J. ASTM Int. (JAI) 5 (3) (2008) 1–20. JAI101257.

[11] B. Hutchinson, B. Lehtinen, A theory of resistance of Zircaloy to uniform corrosion, J. Nucl. Mater. 217 (1994) 243–249.

[12] E. Polatdis, P. Frankel, J. Wei, M. Klaus, R. Comstock, A. Ambard, S. Lyon, R. Cottis, M. Preuss, Residual stresses and tetragonal phase fraction characterization of corrosion tested zircaloy-4 using energy dispersive synchrotron X-ray diffraction, J. Nucl. Mater. 432 (2013) 102–112.

[13] D. Spengler, Evolution of the oxide microstructure and oxide growth induced residual strains during waterside corrosion of zirconium alloys, M.S. Thesis, in: Nuclear Engineering, The Pennsylvania State University, 2012.

[14] D.J. Spengler, A.T. Motta, R. Bajaj, J.R. Seidensticker, Z. Cai, Characterization of Zircaloy-4 corrosion films using microbeam synchrotron radiation, J. Nucl. Mater. 464 (2015) 107–118.

[15] B.M. Ensor, A.T. Motta, R. Bajaj, J.R. Seidensticker, Z. Cai, XANES analysis of iron in Zircaloy-4 oxides formed at different temperatures studied with microbeam synchrotron radiation, in: Porceedings of the ANS LWR Fuel Performance Meeting, TopFuel, 2015 paper A0191, 2015.

[16] R. Bajaj, B.F. Kammenzind, D.M. Farkas, Effects of neutron irradiation on the microstructure of alpha-annealed Zircaloy-4, in: Zirconium in the Nuclear Industry: Thirteenth International Symposium vol. 1423, ASTM STP, 2001, pp. 400–426.

[17] B.F. Kammenzind, K.L. Eklund, R. Bajaj, The influence of in-situ clad straining on the corrosion of Zircaloy in a PWR water environment, in: Zirconium in the Nuclear Industry: Thirteenth International Symposium vol. 1423, ASTM STP, 2002, pp. 524–560.

[18] K.R. Anderson, R. Bajaj, Microstructural and microchemical analyses of extracted second-phase precipitates in alpha-annealed and beta-quenched zircaloy-4, Microsc. Microanal. 20 (2014) 500–501.

[19] J.A. Gruber, S.A. Brown, G.A. Lucadamo, Generalized Kearns texture factors and orientation texture measurement, J. Nucl. Mater. 408 (2) (2011) 176–182.

[20] W.S. Rasband, ImageJ, U.S.National Institutes of Health, Bethesda, Maryland, USA, 1997-2014. http://imagej.nih.gov/ij/.

[21] A. Hammersley, S. Svensson, M. Hanfland, A. Fitch, D. Hausermann, Two-dimensional detector software: from real detector to idealised image or two-theta scan, High Press. Res. 14 (1996) 235–248.

[22] PeakFit 12 ed, 4, Systat Software Inc., 2012.

[23] B. de Gabory, A.T. Motta, K. Wang, Transmission electron microscopy characterization of Zircaloy-4 and ZIRLO oxide layers, J. Nucl. Mater. 456 (2015) 272–280.

[24] R. Garvie, P. Nicholson, Phase Analysis in zirconia systems, J. Am. Ceram. Soc. 55 (1972) 303–305.

[25] J.-Y. Park, H.-G. Kim, Y.H. Jeong, Y.-H. Jung, Crystal structure and grain size of Zr oxide characterized by synchrotron radiation microdiffraction, J. Nucl. Mater. 335 (2004) 433–442.

[26] A.T. Motta, A. Yilmazbayhan, R.J. Comstock, J. Partezana, G.P. Sabol, B. Lai, Z. Cai, Microstructure and growth mechanism of oxide layers formed on Zr alloys studied with micro-beam synchrotron radiation, J. ASTM Int. (JAI) 2 (5) (2005) 1–26.

[27] R.C. Garvie, The occurrence of metastable tetragonal zirconia as a crystallite size effect, J. Phys. Chem. 69 (4) (1965) 1238–1243.

[28] R.C. Garvie, M.F. Goss, Intrinsic size dependence of the phase transformation temperature in zirconia microcrystals, J. Mater. Sci. 21 (1986) 1253–1257.

[29] H. Li, M. Glavicic, J. Szpunar, A model of texture formation in ZrO2 films, Mater. Sci. Eng. A 366 (2004) 164–174.

[30] G. Lucadamo, J. Gruber, Investigating the influence of zircaloy-4 grain orientation on oxide corrosion films formed in an autoclave environment, Microsc. Microanal. 23 (S1) (2017) 2200–2201.

[31] H. Swan, M.S. Blackmur, J.M. Hyde, A. Laferrere, S.R. Ortner, P.D. Styman, C. Staines, M. Gass, H. Hulme, A. Cole-Baker, P. Frankel, The measurement of stress and phase fraction distributions in pre and post-transition Zircaloy oxides using nano-beam synchrotron X-ray diffraction, J. Nucl. Mater. 479 (2016) 559–575.